Applied Catalysis B: Environmental 300 (2022) 120711

Contents lists available at ScienceDirect

Applied Catalysis B: Environmental

journal homepage: www.elsevier.com/locate/apcatb

Partial oxidation of isobutylene using Ni TiO_x

Seth March [a], Luisa F. Posada [a], Inosh Perera [a], Tharindu Kankanam Kapuge [a], Vera Grankina [b], Partha Nandi [b,*], Steven L. Suib [a,c,**]

[a] Department of Chemistry, University of Connecticut, 55 North Eagleville Road, Storrs, CT 06269, United States
[b] Corporate Strategic Research, ExxonMobil Research and Engineering Company, 1545 US 22 East, Annandale, NJ 08801, United States
[c] Institute of Materials Science, University of Connecticut, 91 North Eagleville Road, Storrs, CT 06269, United States

ARTICLE INFO

Keywords:
Partial oxidation
Heterogeneous catalysis
Isobutylene
Ni titania
p-xylene

ABSTRACT

We report an aerobic partial oxidation of isobutylene into isoprene, acetone, and para-xylene using a mesoporous Ni TiO_x catalytic material. In this work, two catalysts were found to synthesize two of these three valuable products with high selectivity, with *p*-xylene being synthesized with a selectivity of 46.0% and isoprene being synthesized with a selectivity of 64.7%, with overall conversions of isobutylene being 34.0% and 11.9% respectively. These reactions were done at relatively low temperatures (300 °C or below) and are conducted at flow rates of 10 sccm oxygen and isobutylene. The nickel titania catalysts were studied extensively using various characterization methodologies such as TEM, Raman, XRD, and XRF.

1. Introduction

The partial oxidation of hydrocarbons using molecular oxygen as an oxidant is vital due to products of such reaction being precursors of valuable products [1–3]. One hydrocarbon of interest is isobutylene which can be obtained from natural gas liquid (NGL) streams and fluid catalytic cracking (FCC), which can be used to synthesize valuable products [4]. Isobutylene is typically converted into jet fuel, high octane gasoline, and high octane additives such as MTBE. In this manuscript, we focus our attention on the partial oxidation route of isobutylene for making valuable chemicals. In this partial oxidation reaction, the most prominent products are methacrolein, *p*-xylene, isoprene, acetone, CO, and CO_2 [5–9]. The most interesting of the products being methacrolein, *p*-xylene, and isoprene. These products are of interest as they can be used synthesize polymers and other valuable materials [10–16]. Typically the first two products can be synthesized using partial oxidation, however, isoprene, can be made when isobutylene undergoes a condensation reaction [9,16–18]. Usually the toxic substance formaldehyde is necessary to form isoprene [17,19–22].

Typically the process of oxidizing isobutylene is done via expensive routes, such as using gold as a catalyst [6,23]. Some inexpensive catalysts that have been found to carry out this oxidation reaction are mixed metal oxides, typically using molybdenum or bismuth as the metals [24–26]. The conversions for these reactions were in the range of 10–60% at 420 °C when the ratio of oxygen to isobutylene was 1:1 [24–26]. However for these experiments *p*-xylene and isoprene were not seen. Some experiments have been done from isobutylene to *p*-xylene where using a chromium oxide catalyst, isobutylene can be converted to *p*-xylene with ~ 18.7% yield at 500 °C [27].

Aside aforementioned catalysts, titanium dioxide (titania) has shown activity for partial oxidation of isobutylene to methacrolein, isobutylene oxide, isobutane, and acetone in an ultra-high vacuum (UHV) setting [6]. However, the overall conversion of this reaction at atmospheric pressure is low [6]. Using dopants has been found to facilitate this reaction at atmospheric pressure at a much higher conversion, where when gold or uranium were added to TiO_2 the conversions to methacrolein increased from 10% to 35% at 600 °C [6,28].

Since titania is already known as a proficient support in the partial oxidation of methane, the characteristics of that reaction might transfer over to the partial oxidation of a higher-ordered hydrocarbon [29]. Similarly to the oxidation of isobutylene, when titania is doped with other metals, the overall isobutylene conversion increases. One such metal that is a cheap alternative to the afore-mentioned precious metals, is nickel due to its small particle size [30–33] and stronger metal-support interactions [30–35]. Additionally, nickel is known to dimerize ethylene as opposed to going through a polymerization pathway, and if isobutylene gets dimerized, then cyclization into *p*-xylene could occur, making Ni an interesting dopant for this reaction

* Corresponding author.
** Corresponding author at: Department of Chemistry, University of Connecticut, 55 North Eagleville Road, Storrs, CT 06269, United States.
E-mail addresses: partha.nandi@exxonmobil.com (P. Nandi), steven.suib@uconn.edu (S.L. Suib).

https://doi.org/10.1016/j.apcatb.2021.120711
Received 28 June 2021; Received in revised form 25 August 2021; Accepted 7 September 2021
Available online 13 September 2021

[36]. In previous research in our group tunable mixed metal oxides have synthesized and found to be able break allylic bonds, making a mixed Ni TiO_x system possible [37–41]. The goal of this work is to expand that research to break the allylic bonds of isobutylene, and discover what valuable products can be synthesized by using a Ni TiO_x catalyst. The addition of nickel aids in the formation of the rarer products isoprene and *p*-xylene at 300 °C.

2. Experimental

2.1. Sample synthesis

All precursors were bought from Sigma-Aldrich. The mixed metal oxide of nickel and titanium (Ni TiO_x) was synthesized by a modified doped University of Connecticut (UCT) synthesis method described in previous literature [39,40]. Here, varying amounts (0.001–0.01 mol) of nickel nitrate hexahydrate ($Ni(NO_3)_2{\cdot}6\ H_2O$) were dissolved in 0.23 mol of 1-butanol in a 150 mL beaker via magnetic stirring. Then 0.034 mol of 15.8 M nitric acid (HNO_3) was added to the stirred solution. Lastly, 0.02-x (where x is the amount of nickel precursor used) mol of titanium (IV) butoxide ($Ti(OCH_2CH_2CH_2CH_3)_4$) and 0.0043 mol of P123 (poly (ethylene glycol)-block-poly(propylene glycol)-block-poly(ethylene glycol) were added into the solution and stirred until homogenous. The solution was then heated at 120 °C for 3 h and the resulting material was calcined in two different ways. After the initial heating, the material in the 150 mL beaker can be gel-like or powder-like with a yellow tint. With higher amounts of titanium precursor, the material will be gel like, and with higher amounts of the nickel precursor the material will be powder-like. Powder- like materials were washed in ethanol and centrifuged 5 times at 7000 RPM, the washed blue material was then placed in a vacuum oven to dry overnight at room temperature. The dried material was then calcined at 150 °C for 12 h, 250 °C for 3 h, and 350 °C for 2 h, each with a ramp rate of 10 °C per minute. The gel-like material is directly heated at a rate of 2 °C per minute and held at 450 °C for one hour. Five nickel catalysts were synthesized being 1%, 5%, 10%, 20%, and 50% Ni TiO_x. From XRF seen in Table 5, the molar loading does not equal the actual percent loading, in which we see that the five catalysts being made are: 1.5%, 6.9%, 14.1%, 24.6%, and 33.1%Ni TiO_x.

2.2. Catalytic reaction

Two gas cylinders, one filled with 5% isobutylene balanced in nitrogen and the other filled with 5% oxygen balanced in nitrogen, were flowed into a mass flow controller (MFC) at varying flow rates (between 1 and 20 sccm). This gaseous mixture flowed into a straight quartz tube with a 1/8th inch outer diameter. The catalyst was placed in the quartz tube and held with quartz wool, and then the tube was placed in a programmable tube furnace attached to a cold trap submerged in dry ice to collect any liquid products. Initial runs to determine what gaseous products were formed were analyzed with a Gas Chromatography-Mass Spectrometer (GC-MS), equipped with three Haysep A columns and two molecular sieve columns. When CO was not detectible in the reaction, future experiments had their gas products analyzed by a separate gas chromatography (GC) instrument, equipped with a molecular sieve column. This process and apparatus can be seen in Fig. S1. In the standard reaction, 100 mg of catalyst, 10 sccm of isobutylene and oxygen, were heated to 300 °C at a ramp rate of 10 °C per minute for 4 h. The gas conversion was calculated using the ratio between isobutylene and balanced nitrogen in a blank run and comparing to the ratio between isobutylene and the same concentration of balanced nitrogen during the reaction, as seen in Eq. (1). CO_2 selectivity was determined using Eq. (2). Liquid products and selectivity were determined by GC-MS methods via concentration. These conversions and their selectivity were compared to a mass balance seen in Table S1 and Eq. (S1), which for 33.1% Ni TiO_x the mass balance was ~ 99.3%.

$$\text{Isobutylene}(C_4H_8)\text{conversion}(\%) = \frac{\frac{C_4H_{8blank}}{N_{2blank}} - \frac{C_4H_{8sample}}{N_{2sample}}}{\frac{C_4H_{8blank}}{N_{2blank}}} * 100 \quad (1)$$

$$CO_2 \quad \text{Selectivity}(\%) = \frac{\frac{C_4H_{8blank}}{N_{2blank}} - \frac{CO_{2\ sample}}{N_{2\ sample}}}{\frac{C_4H_{8blank}}{N_{2blank}}} * 100 \quad (2)$$

2.3. Reaction procedure of partial oxidation of isobutylene by various oxidants

The 5% isobutylene balanced in nitrogen mixture was flowed into a bubbler filled with the oxidant of choice (water, dimethoxymethane, methanol, 1,3,5-trioxane). Because of the similarities of the densities of the liquids (0.8–1.2 g/mL), all used the same sccm of 5% Isobutylene bubbling in. The gaseous mixture then flowed into a quartz tube reactor loaded with catalyst and was heated to 300 °C by a programmable tube furnace. If oxygen was needed for the reaction, the oxygen and isobutylene mixtures were combined and then flowed into the bubbler and into the quartz tube. This procedure and apparatus can be seen in Fig. S2.

2.4. Characterization

Thermogravimetric analysis-mass spectrometry (TGA-MS) was done on the post calcined catalysts to determine how heat affects the catalyst during the reaction. About 20 mg of catalyst was heated from room temperature to 900 °C at a rate of 10 °C per minute. Oxygen (5 sccm) and 45 sccm of argon were flowed onto the catalyst to imitate reaction conditions. The Mass Spectrometer was used to detect any gaseous species coming off the catalyst during heating. Samples were analyzed with a TG 209 F1 Libra thermogravimetric analyzer attached with a QMS 403C quadrupole mass spectrometer. CO_2 TGA was also done to understand catalyst stability. In which ~ 25 mg of sample was heated to 300 °C over 50 sccm of CO_2 and 50 sccm of N_2.

The thermal stability of the sample was determined by Differential scanning calorimetry (DSC), where 20 mg of catalyst was heated from 25 °C to 900 °C at a flow rate of 20 °C per minute. A flow of 100 sccm of argon was used over the catalyst during the heating. A SDT Q-60 was used for these experiments.

The carbonaceous species coming off the post-reaction catalysts were studied with temperature- programmed desorption (TPD). This was done using a Hiden Analytical HPR-20 R&D gas analysis system, attached with a triple filter mass spectrometer to analyze gases coming off in real- time. In a typical experiment, about 100 mg of sample was placed in a 1/8th inch (inner diameter) quartz tube and heated from 25 °C to 600 °C with a ramp rate of 10 °C per minute with 25 sccm of helium being flowed during the heating. The Mass Spectrometer was used to detect any gaseous species coming off the catalyst during heating.

Metal dispersion was identified by H_2 TPD. A Hiden Analytical HPR-20 R&D gas analysis system was used. Before analyzing, roughly 100 mg of sample was placed in a 1/8th inch (inner diameter) quartz tube and reduced in hydrogen at 300 °C for 30 min. After this, argon was flowed over the sample to ensure hydrogen analyzed was chemisorbed hydrogen. TPD experiments were done starting at 25 °C and gradually heated up to 600 °C over a period of an hour with 25 sccm of argon being flowed during this process.

Elemental quantification was established by using X-ray fluorescence (XRF), where 50 mg of sample is placed in a 10 mm (inner diameter) sample container. Samples are then placed in a metal holder and placed into the instrument. This is conducted via a Rigaku ZSX Primus IV sequential wavelength-dispersive XRF spectrometer (4 kW Rh anode).

Morphology and elemental mapping were studied via Transmission electron microscopy (TEM). An FEI, Talos F200X microscope was used, which was operated with a 200 kV voltage, attached with an Energy Dispersive X-ray spectroscopy (EDS) detector for elemental mapping. TEM grids were prepared by suspending 1 mg of sample in 2 mL of ethanol, sonicating for 1 min, then dispersing liquid on a carbon/copper grid.

The surface area and the porosity of the catalyst were determined by Brunauer-Emmett-Teller (BET) and Barrett-Joyner-Halenda methods, respectively. Samples of 100 mg were placed in a BET tube, then degassed at 150 °C for 6 h. This was done to remove species that are physically adsorbed to the catalyst.

A Rigaku Ultima IV Powder Diffractometer, using Cu Kα ($\lambda = 1.5406$ Å) radiation, was used to determine the crystallinity and crystal phases of the catalyst. The beam current was set at 40 mA, and the beam voltage was set to 45 kV. The scanning 2θ range was set to 5–80°, with a scan rate of 2.0°/min.

Raman spectra were obtained with a Renishaw 2000 Raman scope (0.024 in. focus length, 1800 mm^{-1} grating) attached with a CCD detector powered by a 514 nm wavelength laser. Samples were prepared by putting 1 mg of sample on a glass slide and putting it in the instrument.

A SRI 8610C gas chromatography (GC) instrument was used to identify the concentration of CO_2, isobutylene, and nitrogen. Two Haysep B columns were used, with a flow rate of 30 PSI of helium as a carrier gas, and gases were heated to 250 °C at a ramp rate of 10 °C per minute.

A gas chromatography-mass spectrometer (GC-MS) was used to identify liquid reaction products. This was done using an Agilent 5977B GC/MSD instrument, in which gaseous products were identified using three Haysep A columns and two molecular sieve columns. Gases were heated to 250 °C at a ramp rate of 10 °C per minute. Two CP-Wax 52 CB columns with a 30 m length, 0.32 mm inner diameter, and 1.0 μm film thickness were used to identify liquid products. One μL of the sample was injected into the GC-MS column and heated to 250 °C at a rate of 10 °C per minute.

Nuclear Magnetic Resonance (NMR) spectroscopy was used to determine liquid products made during the catalytic reactions. Said spectrometer was a Bruker Avance III 400 MHz NMR Spectrometer, equipped with a 5 mm BBFO probe used to attain ^{1}H and ^{13}C spectra.

3. Results

3.1. Optimization of reaction parameters

When this reaction was conducted, the products seen were CO_2, acetone, methacrolein, isoprene, *m*-Xylene, and *p*-Xylene. These products were analyzed via NMR, GC, and GC-MS results. All reactions were done using the setup seen in Fig. S1, unless stated otherwise. Initial studies done on the 33.1% Ni TiO_x catalyst can be seen in Fig. 1a, in

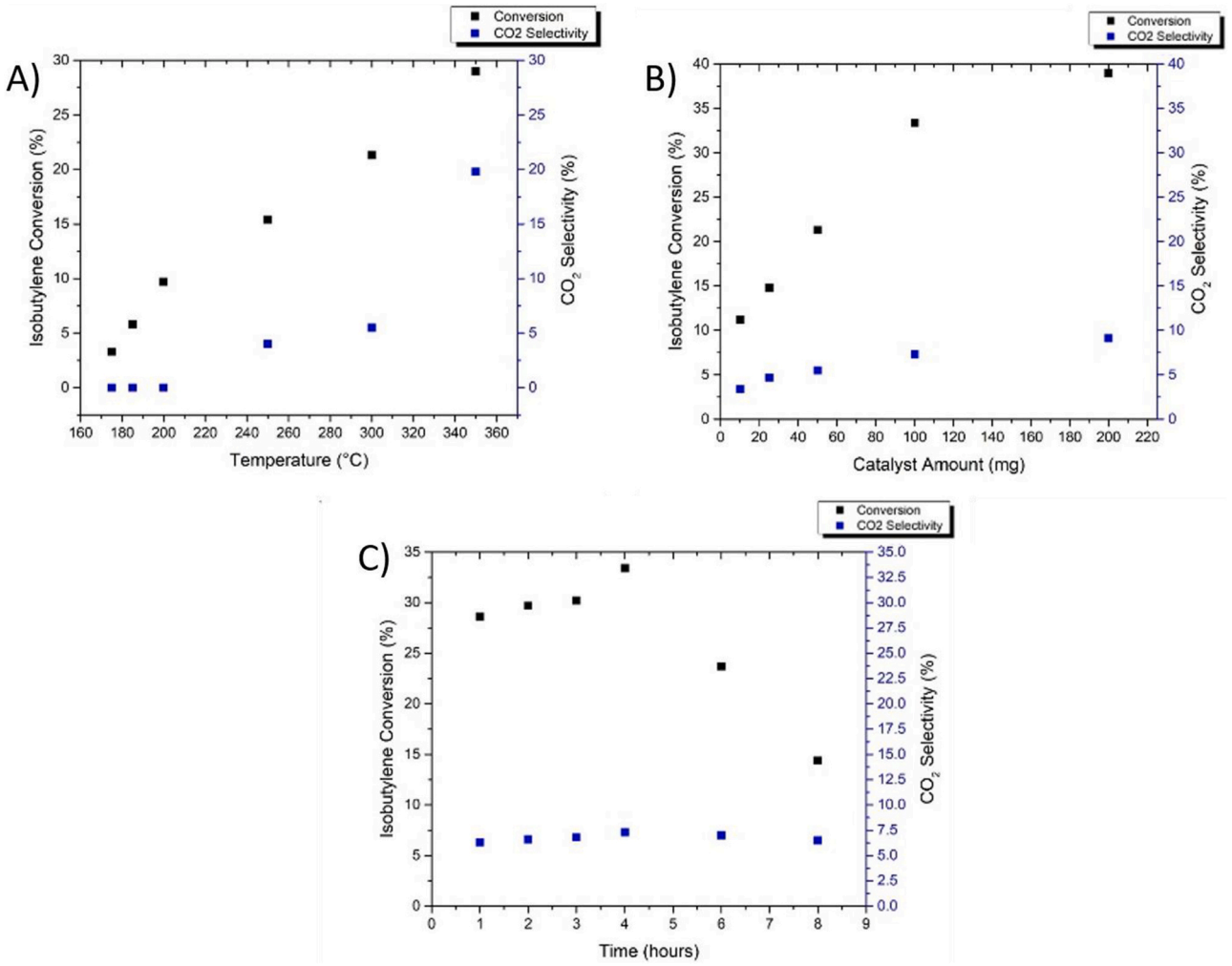

Fig. 1. (a) Temperatures effects on conversion for 50 mg of 33.1% Ni TiO_x with 10.0 sccm of isobutylene and oxygen being flowed after four hours, (b) Amount of catalyst effect on conversion for 33.1% Ni TiO_x at 300 °C with 10.0 sccm of isobutylene and oxygen being flowed after four hours, (c) The effect of time on 100 mg of 33.1% Ni TiO_x, at 300 °C with 10.0 sccm of isobutylene and oxygen being flowed.

which the role of temperature was studied. The temperature started at 175 °C with a flow rate of a 10.0 sccm for both isobutylene and oxygen, which was flowed over 50 mg of 33.1% Ni TiO_x. Initially, at 175 °C there is a 3.3% conversion with no observed CO_2. As the temperature increases, so does the conversion; however, with 185 °C and 200 °C, CO_2 is still not produced. At 250 °C, CO_2 is observed with a selectivity of 4.0%. Above 250 °C, both the conversion and selectivity increase with temperature. No production of CO was seen in any reactions. Future reactions were run at 300 °C, which gave the highest ratio of valuable liquid products to CO_2 compared to total conversion (21.3% conversion and CO_2 selectivity of 5.5%).

To further optimize the reaction, the amount of catalyst and its effect on conversion/selectivity was studied in Fig. 1b. An increased amount of catalyst leads to both a higher selectivity and conversion. With 10 mg of 33.1% Ni TiO_x, the lowest conversion and CO_2 selectivity of 11.2% and 3.4% are observed, respectively. The highest overall conversion was seen to be 39.0%, with 200 mg of catalyst being used and a CO_2 selectivity of 9.1%. However, future reactions were done at 100 mg which gave the highest ratio of liquid products to CO_2, which is shown in Fig. 1b.

The effect of gas flow is shown in Table 1, where the flow rate of one gas was varied, and the other gas had a constant flow rate of 10 sccm. When 10.0 sccm of both oxygen and isobutylene were flowed, the conversion of isobutylene to products was 33.4%. When the amount of oxygen was decreased/increased, so did both the CO_2 selectivity and overall conversion decreased/increased. When the flow rate of oxygen was constant at 10 sccm, and the isobutylene flow rate decreased, again the conversion and CO_2 selectivity decreased. However, when the flow rate increased to 15.0 and 20.0 sccm, the conversion decreased, and the CO_2 selectivity increased. This shows that the optimum flow rate of the two gases is a 1:1 mixture of isobutylene and oxygen being flowed at 10 sccm each. Flowing experiments were done using these parameters to maximize the yield of liquid products.

In Fig. 1c, the time dependence for the conversion and selectivity of the catalyst is shown. For the first four hours of the reaction, the conversion and CO_2 selectivity increase, peaking at 33.4% and 7.3%, respectively. As the reaction goes longer than 4 h, the conversion and CO_2 selectivity decrease. The conversion of isobutylene terminates at around 14%, thus showing that the catalyst gets slightly deactivated during the reaction.

3.2. Nickel loading and its effect on conversion/selectivity

The effect of nickel on isobutylene conversion is shown in Table 2. Initially, with no nickel added, a pure TiO_2 has a conversion of 1.50%. This conversion increases as more nickel is added. With 1.5% Ni TiO_x the conversion increased from 2.1% to 7.5%. This trend continues with 6.9%, 14.1%, 24.6%, and 33.1% Ni TiO_x having conversions of 8.7%, 11.9%, 18.0%, and 33.4% respectively. Table 2 suggests that CO_2 selectivity increases with nickel amount, with the CO_2 selectivity increasing from 1.6% to 7.3% when the nickel amount is increased from 1.5% to 33.1%. With pure NiO_x, the conversion is 4.2% which is lower than any of the Ni TiO_x catalysts. However, pure nickel has a very high CO_2 selectivity. The highest selectivity seen is from 14.1% Ni TiO_x showing a selectivity of 64.7% towards isoprene, and 33.1% Ni TiO_x shows a selectivity of 46.0% towards *p*-xylene.

Table 1
The effect of gas flow on 100 mg of 33.1% Ni TiO_x, at 300 °C, where parentheses indicate molar ratio to the secondary gas.

Sample	Conversion (%)	CO_2 selectivity (%)
2.5 sccm O_2(1:4)[1]	7.0	2.4
5.0 sccm O_2(1:2)[1]	10.5	2.8
10.0 sccm O_2(1:1)[1]	33.4	7.3
15.0 sccm O_2(3:2)[1]	26.5	6.4
20.0 sccm O_2(2:1)[1]	18.0	4.6
2.5 sccm Isobutylene (1:4)[2]	6.5	2.5
5.0 sccm Isobutylene (1:2)[2]	14.2	3.3
10.0 sccm Isobutylene (1:1)[2]	33.4	7.3
15.0 sccm Isobutylene (3:2)[2]	25.0	17.5
20.0 sccm Isobutylene (2:1)[2]	15.7	25.0

Where [1] had isobutylene at a constant 10.0 sccm and [2] had oxygen at a continuous 10.0 sccm. The reaction was run until maximum conversion was calculated, which was at 4 h.

The overall highest selectivity seen for these reactions was a 64.7% selectivity towards isoprene for the 14.1% Ni TiO_x catalyst. Because of this high selectivity, the effects of changing reaction temperature were tested for this specific catalyst. As seen in Table 3, when the reaction was 100 °C there was no conversion to products. When the temperature increased to 150 °C, the conversion increased to 0.5%, with only isoprene and acetone were observed. At 200 °C, the conversion was 2.5% and all products but methacrolein could be seen. At 250 °C, the conversion increased to 7.8% of all products with an isoprene selectivity of 50.7%. The highest conversion came from 300 °C, with an 11.9% conversion and an isoprene selectivity of 64.7%. Higher temperatures were not used since Fig. 1a suggests that higher temperatures promote total oxidation to CO_2. Similar to Fig. 1a, the increase of temperature yields a higher overall conversion and an increased CO_2 selectivity.

The role of the oxidant was also tested to observe if other oxygen sources could convert isobutylene into products. Dimethoxymethane (DMM), methanol, water, and 1,3,5-trioxane were tested using the setup in Fig. S.2. Methanol and DMM were used in particular to see if they could be used as formaldehyde precursors. While there were conversions for these oxidants, they were minimal (< 5.0%), and no additional products were observed that were not seen in Table 3. The lack of conversion for these reactants implies that formaldehyde is being produced in situ during the partial oxidation reaction.

3.3. Material characterization

The changing of the surface area with the addition of nickel was studied using Brunauer-Emmett- Teller (BET) methods, which can be seen in Table 4. With the addition of nickel, the surface area increases. The initial TiO_2 sample has a surface area of 67 m^2/g, and NiO has a surface area of 100 m^2/g. When nickel is loaded into the catalyst, the surface area increases from 67 m^2/g, and 33.1% Ni TiO_x has the highest surface area of 372 m^2/g, which is more than double the next highest surface area. From the BJH pore size distribution, which is seen in Fig. S3, all the Ni TiO_x catalysts are monomodal. From the BET isotherms seen in Figs. S4–S8, every catalyst has a type IV isotherm H2 hysteresis loop, which indicates mesoporous materials.

With the use of X-ray Fluorescence (XRF), the amounts of nickel and titanium in the bulk of the catalyst were identified, as seen in Table 5. The proposed nickel amounts, if they were equal to the loaded amount of nickel, should be 1%, 5%, 10%, 20%, and 50%. For the first four catalysts, the loaded nickel amount is close to the actual nickel amount. However, this is not the case for the catalyst with 50% loaded Ni; in actuality this material has 33.1% nickel in the catalyst.

Energy Dispersive X-ray Spectroscopy (EDX) was also able to determine the percentage of nickel particles on separate particles of the catalyst, which can be seen in Table 5. For all catalysts aside from 33.1% Ni TiO_x, the percentage amount of nickel on the surface of the catalyst matches the loaded amount of nickel added into the catalyst during synthesis.

The effect of the addition of nickel on the structure of the catalyst was studied by Powder X-ray Diffraction (PXRD), as seen in Fig. 2. With the addition of nickel, a peak starts to appear at 45°. Additionally, the most intense peak at 25°, which correlates to anatase titania's (101) planes, decreases in intensity with the addition of nickel. The peak at 45° seems to correlate with the addition of the Nickel Oxide (NiO) (200) peak, indicating the incorporation of a new phase of NiO. There seems to be peak broadening as more nickel is added, which can be seen in the

Table 2
The effect of nickel loading on conversion, with 100 mg of catalyst and a run time of 4 h at 300 °C with 10.0 sccm of isobutylene and oxygen being flowed.

Sample	Conversion (%)	CO_2 selectivity (%)	Acetone selectivity (%)	Isoprene selectivity (%)	Methacrolein selectivity (%)	*p*-Xylene selectivity (%)	m-Xylene selectivity (%)
TiO_2	2.1	1.2	29.6	44.5	~ 0	24.7	~ 0
NiO	4.2	15.8	36.4	32.7	11.6	3.5	~ 0
1.5% Ni TiO_x	7.5	1.6	37.8	39.0	16.7	4.9	~0
6.9% Ni TiO_x	8.7	1.9	36.3	41.0	14.6	5.8	0.4
14.1% Ni TiO_x	11.9	2.6	24.4	64.7	9.1	1.2	0.6
24.6% Ni TiO_x	18.0	3.5	46.3	13.2	7.8	25.9	3.3
33.1% Ni TiO_x	33.4	7.3	28.6	11.2	2.7	46.0	4.2

Table 3
The effect temperature on the selectivity of isoprene for 14.1% Ni TiO_x, with 100 mg of catalyst and a run time of 4 h at 300 °C with 10.0 sccm of isobutylene and oxygen being flowed.

Sample	Conversion (%)	CO_2 selectivity (%)	Acetone selectivity (%)	Isoprene selectivity (%)	Methacrolein selectivity (%)	*p*-Xylene selectivity (%)	m-Xylene selectivity (%)
14.1% Ni TiO_x 100 °C	~ 0	~ 0	~ 0	~ 0	~ 0	~ 0	~ 0
14.1% Ni TiO_x 150 °C	0.5	1.4	74.9	23.7	~ 0	~ 0	~ 0
14.1% Ni TiO_x 200 °C	2.5	1.7	65.1	26.9	~ 0	5.8	0.5
14.1% Ni TiO_x 250 °C	7.8	2.0	38.5	50.7	7.6	0.8	0.4
14.1% Ni TiO_x 300 °C	11.9	2.6	24.4	64.7	9.1	1.2	0.6

Table 4
Surface area of the Ni TiO_x samples.

Sample	Surface area (m^2/g)	Pore volume (cc/g)	Pore diameter (nm)
TiO_x	67	0.06	3.4
1.5% Ni TiO_x	96	0.09	3.4
6.9% Ni TiO_x	97	0.12	3.4
14.1% Ni TiO_x	126	0.12	3.4
24.6% Ni TiO_x	128	0.20	3.8
33.1% Ni TiO_x	372	0.26	3.8

Table 5
EDX and XRF comparison of: 1.5%, 6.9% Ni TiO_x, 14.1% Ni TiO_x, 24.6% Ni TiO_x, 33.1% Ni TiO_x.

Molar loaded %Ni	XRF Mol %Ni	XRF Mol %Ti	EDX Mol %Ni	EDX Mol %Ti
1% Ni TiO_x	1.5	98.5	1.0	99.0
5% Ni TiO_x	6.9	93.1	6.1	93.9
10% Ni TiO_x	14.1	85.9	8.7	9.3
20% Ni TiO_x	24.6	75.4	20.8	79.2
50% Ni TiO_x	33.1	66.9	48.0	52.0

33.1% Ni TiO_x catalyst, where all but the initial peak is broad.

Transmission Electron Microscopy (TEM) was done to determine the morphology, particle size and locate if there are lattice fringes in the catalysts. These images can be seen in Fig. 3, in which the morphology seems to be nano-spherical. The lower concentration of nickel catalysts seems to have nano-spheroid-shaped morphology, and larger concentrations of nickel have a more well- defined nano-spherical morphology. When zoomed in at a 10 nm scale bar, the particles are 5–10 nm. The 1.5−24.6% Ni TiO_x catalysts seem to be on the larger end of 10 nm, and the 33.1% Ni TiO_x has particles closer to 5 nm. The excess of dark spots on the surface of the catalyst may either be stacking of catalyst on the Z-axis or could be an agglomeration of nickel particles. This was more carefully examined by elemental mapping, as shown in Fig. 4. D-spacings were analyzed for the lattice fringes seen in Fig. 3 (Zoomed in images in Figs. S13–S19), where each of the catalysts showed a similar D-spacing of around 0.35 nm. These lattice fringes are indicative of the (101) planes of anatase TiO_2. Both 24.6% and 33.1% Ni TiO_x catalysts also have lattice fringes due to the (200) planes of NiO, with a D-spacing of around 0.21 nm.

Using Energy Dispersive X-ray Spectroscopy (EDX), the elemental mapping of the TEM images was done as seen in Fig. 4. Nickel particles on 1.5%, 6.9%, and 14.1% Ni TiO_x seem to be dispersed homogeneously throughout the surface of the catalyst, with minimal agglomeration of particles. For 24.6% Ni TiO_x some agglomeration of nickel occurs on one side of the particle. For the 33.1% Ni TiO_x catalyst, the nickel catalyst is homogeneously scattered on the surface of the catalyst. For all the materials, titanium was dispersed throughout the surface of the catalyst, with a minimal agglomeration of titanium particles.

Raman spectroscopy was done to determine how nickel affects the titania structure. As seen in Fig. 5, TiO_2 shows Raman spectra characteristic of anatase titania, with an Eg mode at 144 cm^{-1} and 639 cm^{-1}, a B_{1g} mode at 395 cm^{-1}, and an A_{1g} mode at 516 cm^{-1} [47]. As nickel content increases, the shift for the first E_g also increases, with TiO_x being at 144 cm^{-1} and Ni TiO_x being at 152 cm^{-1}.

When the nickel content reaches 33.1%, the second E_g mode for TiO_2 seems to disappear, and other peaks arise, all correlating to Raman modes in $NiTiO_3$ [46]. The lower intensity modes correspond to vibrations of metal—oxygen bonds [46].

X-ray Photoelectron Spectroscopy (XPS) was conducted on the catalysts to see how the addition of nickel affected the pure titania sample. These data are seen in Figs. (S20–S30). With the addition of nickel, for 1.5% and 6.9% Ni TiO_x, small peaks are seen to correlate with the nickel 2p region. When the nickel content is increased to 14.1%, peaks corresponding to the nickel 2p region are more obviously seen. In Figs. 6, 24.6% Ni TiOx shows peaks correlating to the nickel 2p region, and similar results are observed for the 33.1% catalyst as seen in the Fig. S25. Additionally, from the titanium 2p region seen in Fig. S30, the 33.1% Ni TiO_x sample has an XPS peak indicative of Ti3+ [42]. All of the catalysts have this peak, but 33.1% Ni TiO_x sample has the greatest ratio of Ti3+ to Ti4+ (~ 37.5%).

Differential Scanning Calorimetry (DSC) was done on the catalysts before the reaction to observe how temperature affects the catalyst. From Fig. 7, all the catalysts have their majority mass loss in the

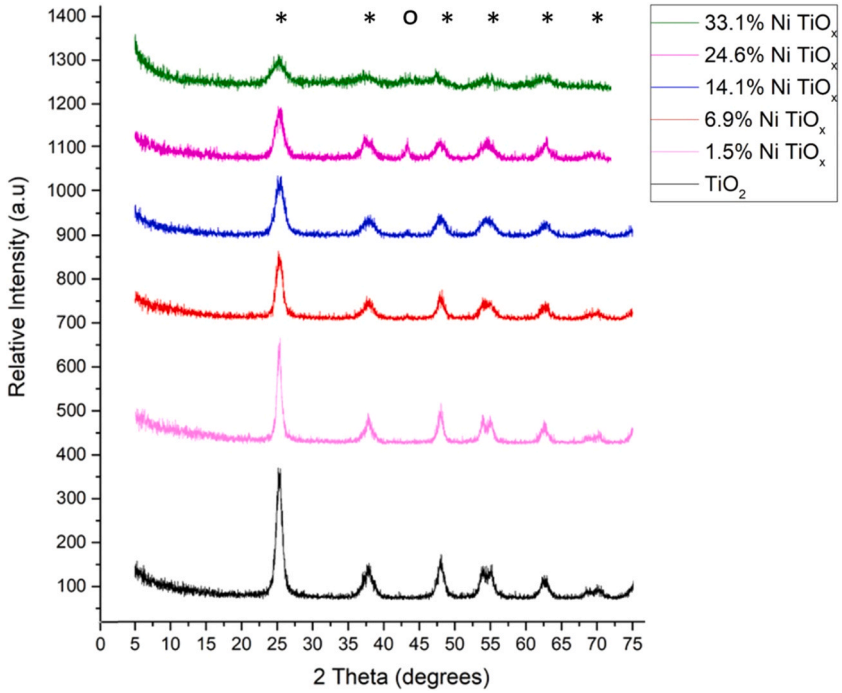

Fig. 2. PXRD the Ni TiO_x catalysts where * is anatase TiO_2, and o is NiO.

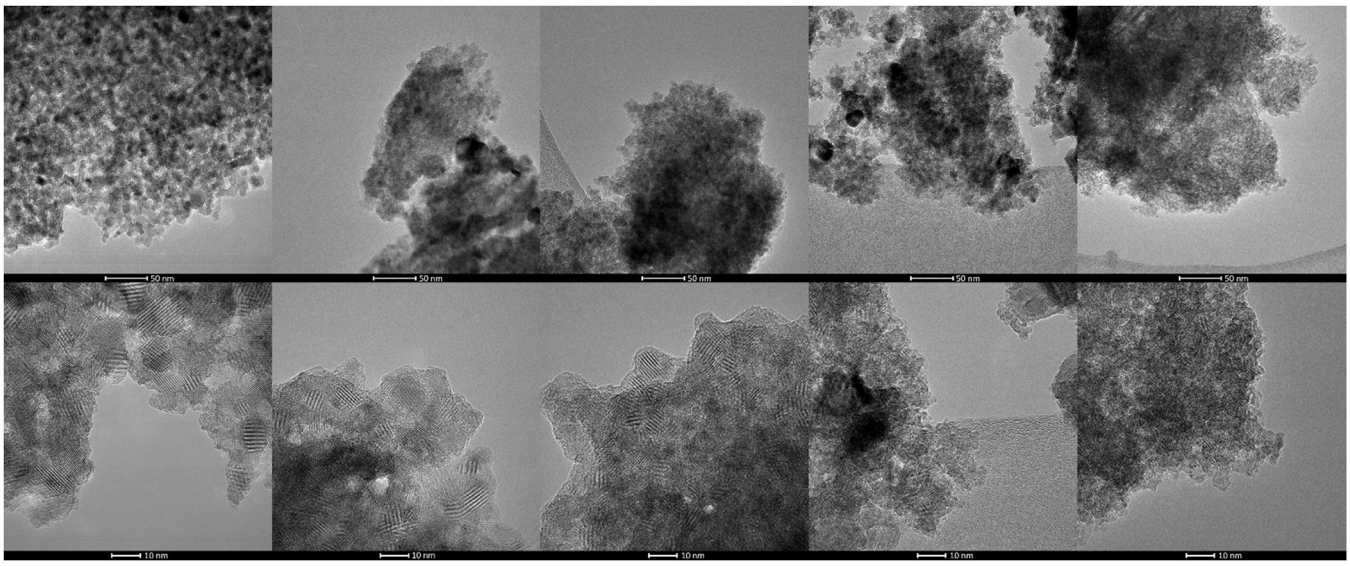

Fig. 3. TEM images from right to left: 1.5% Ni TiO_x 5% Ni TiOx, 14.1% Ni TiOx, 24.6% Ni TiO_x, and 33.1% Ni TiO_x.

100–300 °C region, which is due to loss of water and CO_2 inside the catalyst (seen in Fig. S31). The 33.1% Ni TiO_x has two areas of weight loss, with the second area being from 700 to 800 °C. For 1.5%, 6.9%, and 14.1% Ni TiO_x, here seems to be no correlation between nickel amount and weight loss as 24.6% Ni TiO_x has a smaller weight loss than 14.1% Ni TiO_x, and 33.1% Ni TiO_x has the second-lowest weight loss. Temperature Programmed Desorption (TPD), seen in Fig. S31, was done on 33.1% Ni TiO_x to see what was coming off the fresh catalyst. From there, the first.

weight loss region is due to CO_2 and H_2O, and the second weight loss region at 700 °C is due to O_2, and finally CO_2 starts to come off the catalyst around 600 °C.

3.4. Post-catalytic studies

To understand how the reaction affects the catalyst, post-reaction characterization was done. XRD was used to determine how crystallinity was affected post-reaction, which can be seen in Fig. S32. Similar to the pre-reaction catalysts (Fig. 2), as nickel is increased, a peak at 45° appears, which correlates to NiO (200), and the TiO_2 peaks weaken and get broader. No significant changes are seen between Fig. 2 and Fig. S32.

TEM can be used to see if there were any changes in morphology, elemental dispersion, or if carbonaceous species grew on the catalyst. The morphologies of the catalysts after the reactions can be seen in Fig. S33. Like the pre-reaction TEM images, these catalysts have a nanosphere- like morphology with an apparent diameter of about 5–10 nm. Similar to the pre-reaction catalysts, there are dark spots. No

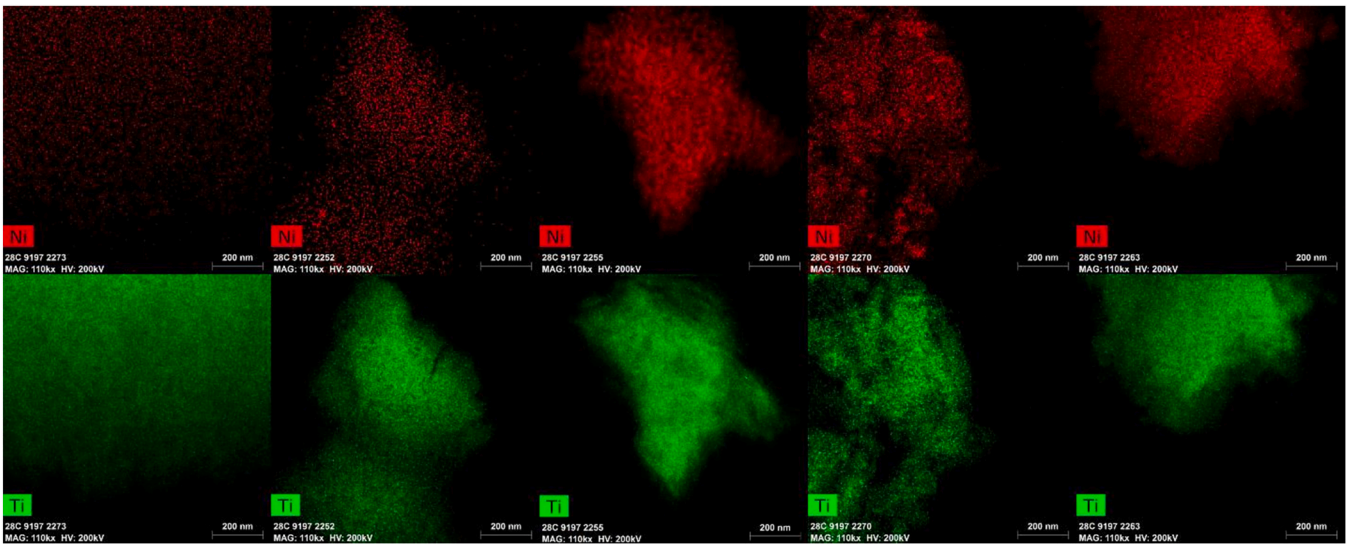

Fig. 4. EDX images from right to left: 1.5%, 6.9% Ni TiO_x, 14.1% Ni TiO_x, 24.6% Ni TiO_x, 33.1% Ni TiO_x.

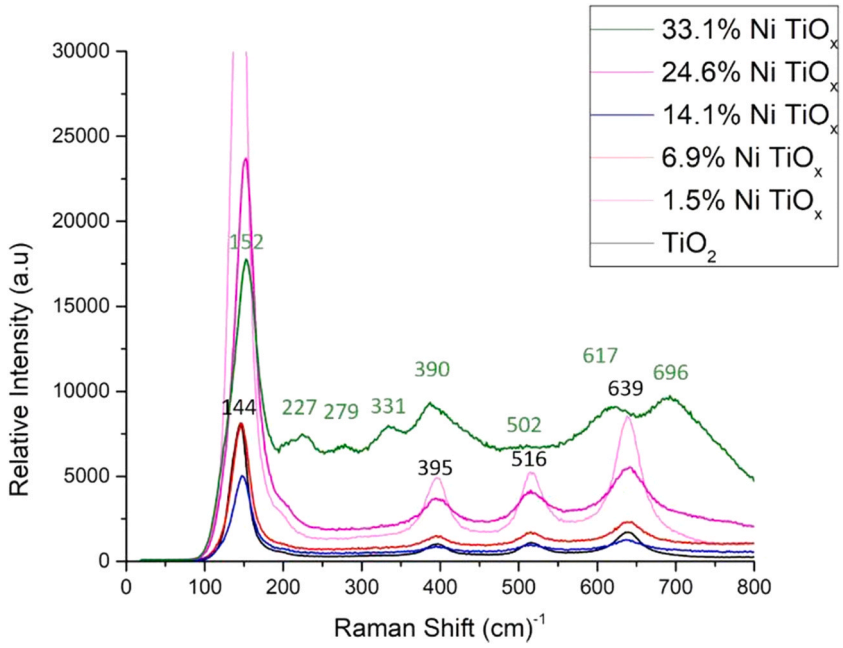

Fig. 5. Raman spectra of Ni TiO_x catalysts.

carbonaceous species are seen on any of the catalysts.

To observe how the nickel particles change during the reaction, EDX was done on the post-reaction catalysts, as seen in Fig. S34. Similar to Fig. 4, the 1.5% Ni TiO_x catalyst is homogeneously dispersed throughout the surface of the catalyst. The 6.9%, 14.1%, and 24.6% Ni TiO_x catalysts show agglomeration of nickel particles on the surface of the catalyst. The 33.1% Ni TiO_x shows a homogenous dispersion of nickel throughout the catalyst. All these catalysts show similar nickel concentrations as compared to their pre-reaction counterpart.

With no carbonaceous species being seen via TEM and minimal understanding as to why the catalyst is being deactivated, Raman spectroscopy was used, as seen in Fig. 8a. Similarly, to the pre-reaction sample, the addition of nickel leads to an increase in the Raman shift for the most intense mode of titania and peak broadening of all the titania modes. Some of the Ni TiO_x catalyst modes disappear after the reaction, most notably the modes that correlate to 279 cm^{-1} and 331 cm^{-1}.

Fig. 8b shows the Raman spectra for 800–2000 cm^{-1}, where two additional modes at 1350 cm^{-1} and 1600 cm^{-1} are observed. These modes correlate to the D and G bands of carbonaceous species [37]. With the catalysts that have higher conversions, greater amounts of carbonaceous species are observed.

XPS was conducted on the used samples to analyze how the oxidation states of nickel change during the reactions (seen in Fig. 9 , Figs. S35-S38). All the catalysts aside from 24.6% Ni TiO_x show similar peaks corresponding to the Ni 2p region as their pre-reaction counterparts. When looking at 24.6% Ni TiO_x there is a peak that appears at around 852 eV, which correlates to Ni^0 [43]. These data suggest that during the reaction, nickel gets reduced from nickel oxide to Ni^0.

To further understand the carbonaceous species on the used catalysts during the reaction, DSC and TPD were conducted. As seen in Fig. 10, except for 33.1% Ni TiO_x, the addition of nickel leads to a higher weight loss. The 33.1% Ni TiO_x catalyst has the same overall weight loss as the 24.6% Ni TiO_x catalyst. Unlike Fig. 7, the main weight loss does not

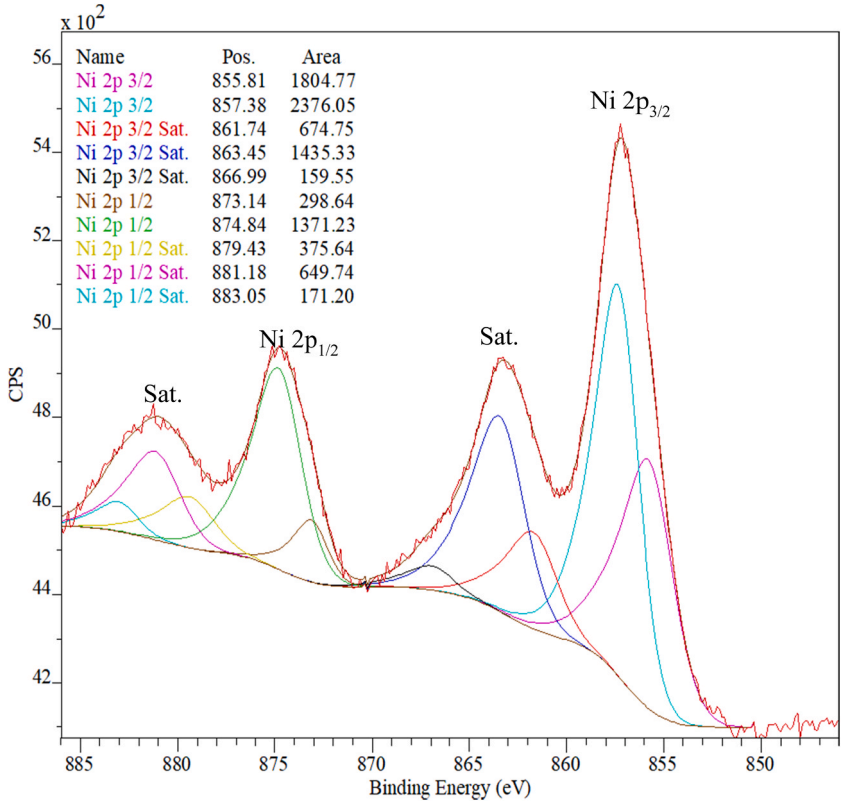

Fig. 6. XPS Spectra of Ni 2p region of 24.6% Ni TiO_x.

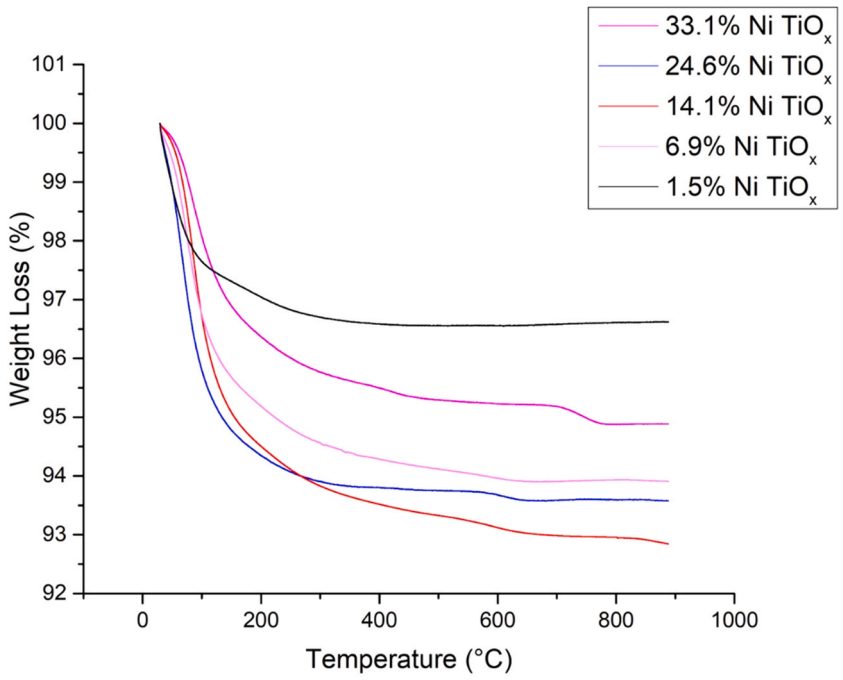

Fig. 7. Differential scanning calorimetry of Ni TiO_x catalysts.

occur from the 100–300 °C region. There is a lower weight loss in this region as compared to their fresh catalyst counterparts. However, there is a much higher overall weight loss for each catalyst. The main weight loss occurs from the 400–600 °C region, and TPD was conducted to determine what species are coming off in this region. The 33.1% Ni TiO_x catalyst has the lowest weight loss in the 100–300 °C region, however, this system has the largest weight loss in the 400–600 °C region.

The TPD can be seen in Figs. S39–S43, where all the catalysts except for 1.5% Ni TiO_x have weight losses that start from 400 °C and are due to CO_2, CO, and H_2O. For Ni TiO_x, this weight loss correlates with CO_2 and CO. The weight loss at 100 °C is due to an initial loss of H_2O and O_2. Isobutylene is not a significant weight loss product except for the case of

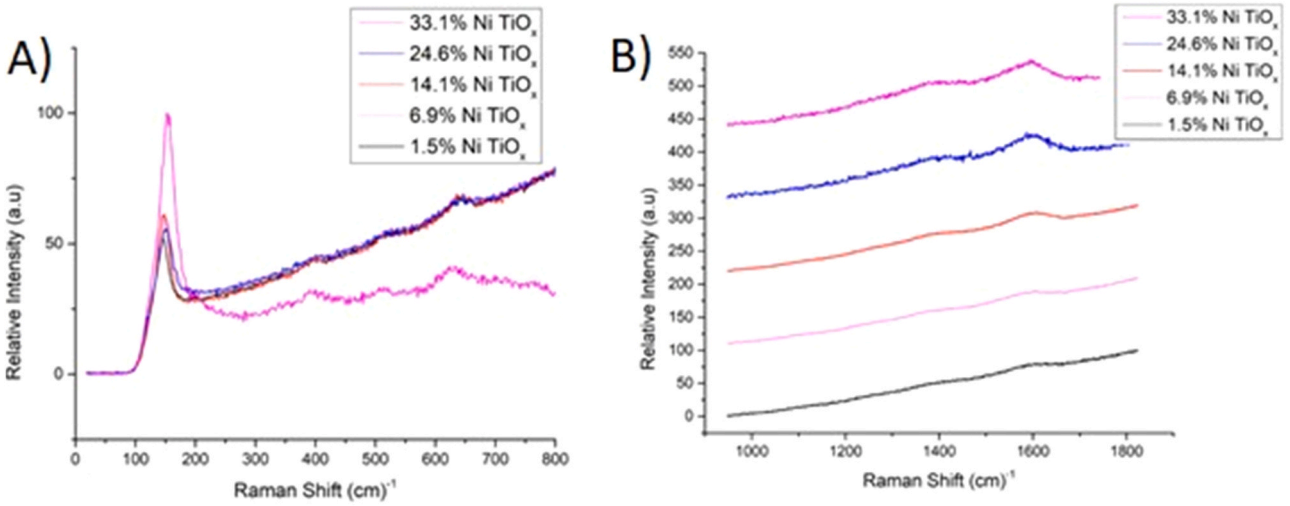

Fig. 8. (a) Raman spectra of used Ni TiO_x catalysts (b) Raman spectra of used Ni TiO_x catalysts in the 800–2000 cm^{-1} region.

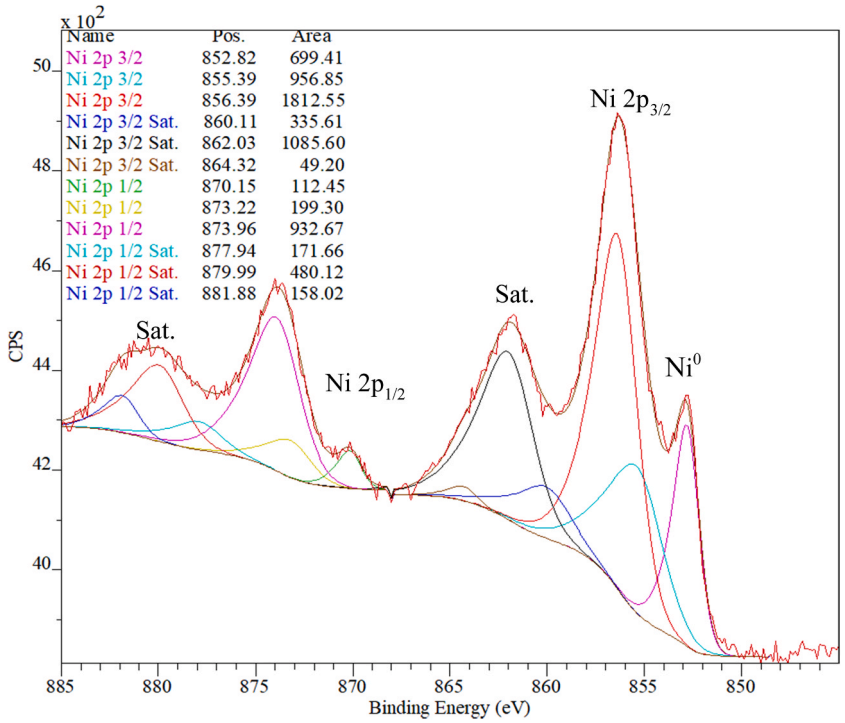

Fig. 9. XPS spectra of Ni 2p region of used 24.6% Ni TiO_x.

33.1% Ni TiO_x, which occurs in the 100 °C region. To identify if the CO_2 coming off the catalyst is poisonous to the reaction, CO_2 TGA was conducted (Fig. S44), where the weight loss caused by CO_2 addition is reversible.

3.5. Catalytic regeneration

From Fig. 1c we observe catalytic deactivation, which occurs after four hours. To ensure that this reaction can be repeated numerous times, catalytic regeneration was attempted, where after the reaction the sample was heated to 450 °C in air overnight. The regenerated catalyst was tested over four hours and re-calcined two additional times to assure the catalyst could be reused. The conversions of the regenerated catalysts were comparable to Fig. 1c, as seen in Table S2.

4. Discussion

4.1. Catalytic reaction

Previously seen products for this reaction have been: CO, CO_2, methacrolein, isoprene, acetone, and xylenes [22–25]. All of these products aside from CO were seen when this reaction was conducted, as seen in Table 2. This suggests that any gaseous products get fully oxidized to CO_2. Xylenes were made at a lower temperature than the aforementioned catalysts, and isoprene was seen without the use of formaldehyde. When formaldehyde was bubbled into the reactor without oxygen, much less product was seen. When the temperature was used as a variable in Fig. 1a, no conversion to CO_2 was observed for temperatures before 200 °C. When the temperature increases, so does both the conversion and CO_2 selectivity, implying that the increased

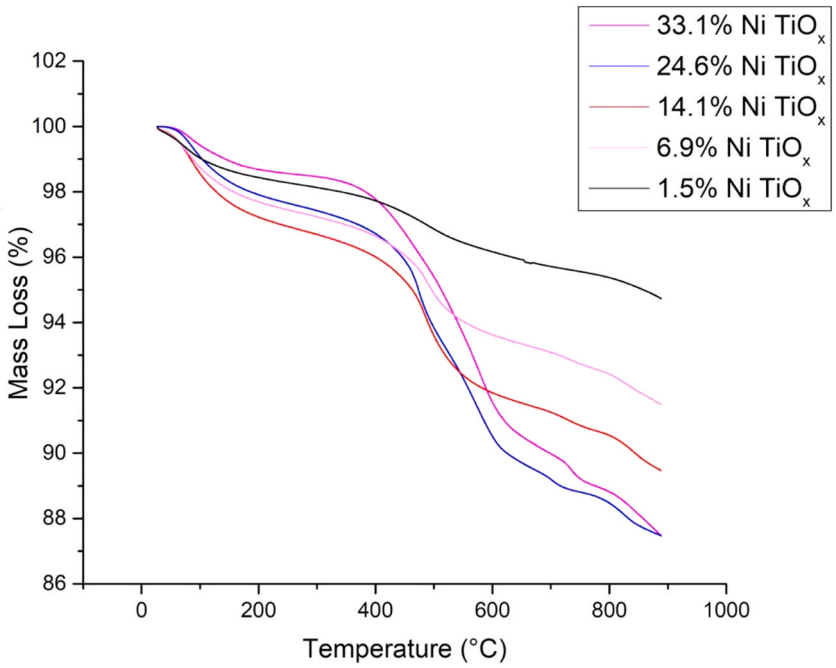

Fig. 10. Differential scanning calorimetry of used Ni TiO_x catalysts.

temperature promotes oxidation (both partial and total oxidation). Catalyst amounts correlate with a higher conversion as well as seen in Fig. 1b, where this effect on conversion somewhat plateaus when a catalyst amount is greater than 100 mg is used. When the gas flow of oxygen is varied, and the isobutylene gas flow is stagnant, the conversion changes, as seen in Table 1. The conversion and CO_2 selectivity trends are the same, in which they increase up to an equal flow to isobutylene (10 sccm) and then decrease when the gas flow further increases. When the amount of isobutylene is varied and oxygen stays the same (10 sccm), the CO_2 selectivity increases with the increase of isobutylene. This indicates that the CO_2 yield is dependent on the amount of the carbon source. The decrease in conversion with the increase of isobutylene after 10 sccm is likely due to increased coking and inability to react all of the isobutylene with limited oxygen. The decrease in conversion after 10 sccm also occurs with oxygen, however this is not due to coking. This decrease is possibly due to the filling of oxygen vacancies faster than isobutylene can react with formed surface oxygen. By not reforming the oxygen vacancies the O_2 adsorption possibly is decreased, thus the conversion may decrease. From 1–4 h, the conversion stays at a similar conversion of ~ 30%. Once the reaction time increases past 4 h, the conversion decreases, as seen in Fig. 1c, which implies catalyst deactivation. However, as seen in Table S2, the catalyst can be regenerated, but the reason for deactivation/regeneration will be further discussed when post-catalytic studies are mentioned. Table 2 shows that the nickel amount correlates with higher conversions, with no trend being seen for nickel loading and selectivity. This is seen for the two catalysts, 14.1% and 33.1% Ni TiO_x where both have high selectivity towards previously mentioned valuable liquid products isoprene and *p*-xylene. These two products are possibly forming via the mechanisms seen in Fig. S45–S46 [17,52]. Since Ni is known to aid in the dimerization process, the higher nickel loading in 33.1% Ni TiO_x leads to *p*-xylene from the cyclization of the dimerized intermediate [44]. Whereas with 14.1% Ni TiO_x the xylenes are not made as with less Ni, there is less dimerization occurring. Instead, this leads to isobutylene reacting with in-situ formed formaldehyde to make isoprene. The two main trends that can be seen are for the lower loaded Ni catalysts, as Ni content goes up the isoprene formation also goes up, possibly due to the increased vacancies observed, which enhances the O_2 adsorption. This enhanced O_2 adsorption possibly allows for the synthesis of formaldehyde from isobutylene and oxygen, which than can interact with isobutylene to form isoprene. Once the loading of Ni reaches 24.1% the dimerization reaction is favored, and when increased to 33.1%, the formation of xylenes is enhanced by this greater amount of nickel. The other trend is CO_2 selectivity, with nickel amount correlating to a higher conversion to CO_2. The 100% nickel loading (NiO) catalyst has the highest selectivity towards CO_2 of 15.8%, suggesting that nickel amount relates to total oxidation. For these Ni TiO_x catalysts, the increasing surface area could be correlated with the higher conversions, as indicated by 33.1% Ni TiO_x having more than double the surface area and conversion than 24.6% Ni TiO_x. However, this correlation does not hold for both the 1.5% and 6.9% and the 14.1% and 24.6% Ni TiO_x catalysts which have similar surface areas, but the conversions are vastly different. While it seems that the role of nickel is to enhance the conversion of the reaction, the role of titania is for O_2 adsorption. Titania is excellent in adsorbing O_2, and this property can be enhanced by the addition of defects [45]. Additional defects were observed in Raman and XPS (Figs. 8 and 9).

4.2. Material characterization

XRF and EDX were both used (Table 5) to see how the weight loading affected the actual percent of nickel in the Ni TiO_x catalysts. For all catalysts except 33.1% Ni TiO_x, the EDX elemental mapping and XRF both agree in that the theoretical nickel loading is equal to the actual nickel loading. For elemental mapping for 33.1% Ni TiO_x, the nickel amount is close to 33.1%, where the XRF for this catalyst is 33.1%, a little under half the amount of the theoretical weight loading. With EDX, the elemental mapping is on a particle-by-particle basis, as well as constricted by the top 100 nm of the particles surface, whereas XRF analyzes the bulk of the catalyst. The difference between the surface and bulk can lead to discrepancies in the percentage, which is likely why the two techniques give different percentages. It is possible that the surface is 50% Ni while the bulk in actuality if 33.1% Ni. However, the reason why the nickel/titanium loading is not the same at the XRF/TEM percentages is due to the washing process. During the washing process, excess metals can be washed away, however this step is necessary to remove all surfactant from the catalyst.

Both XRD and TEM (Fig. 2 and Fig. 3) were done to determine the

effect of nickel on the catalyst structure. When nickel is equally loaded to titanium, the structure seems to become less crystalline than the other catalysts. This is supported by the observation that all the peaks are broader than the other catalysts, and three peaks from 35 ° to 45 ° seem to be fused. Additionally, peak broadening can mean that the overall particle size is getting smaller, which is also seen in the TEM. These smaller particle sizes are beneficial to the reaction, as the smaller particle size increases the surface area. Anatase TiO_2's most intense planes can be seen in the lattice fringes of each catalyst, which can be seen in Figs. S13–S17. For 24.6% and 33.1% Ni TiO_x an additional reflection can be seen from the lattice fringes, which corresponds to the (200) planes of NiO, which agrees with the XRD of this catalyst. No significant changes occur in the d-spacing of the (101) planes of anatase titania with the addition of nickel, as all the catalysts have a similar D-spacing of around 0.35 nm. Dark spots that were seen in the TEM images were analyzed using EDX (Fig. 4) to see if they correlate to clumps of nickel. All catalysts aside from 24.6% Ni TiO_x have homogeneously dispersed nickel throughout the catalyst, meaning that dark spots in the TEM images correlate to the stacking of the catalyst. With 24.6% Ni TiO_x there are agglomerations of nickel seen in the EDX image, and these areas do not relate to an agglomeration of titanium particles, meaning that the small dark clumps in the TEM image are an agglomeration of nickel particles.

Fig. 5 shows the addition of nickel causes a broadening and peak shift in the most intense Raman peak for TiO_2. While there is a shift in the most intense peak, the other three peaks show no peak shift. However, all peaks show broadening with the addition of nickel. Like XRD, the addition of nickel correlates to a broadening of peaks, possibly due to the formation of oxygen vacancies [46]. The new peaks that arise correlate to $NiTiO_3$, which has been found to enhance the interactions between Ni and titania [47]. Furthermore, formation of oxygen vacancies can be inferred from XPS data shown in Fig. 6, where Ti^{3+} is observed, which has been cited to imply oxygen vacancy formation [46]. The formation of oxygen vacancies possibly enhances the conversion by allowing more oxygen to be adsorbed and thus reacted, and the enhanced interactions caused by the $NiTiO_3$ phase could be the reason why 33.1% Ni TiO_x has the best stability of the catalysts.

4.3. Post-catalytic studies

The aforementioned catalyst deactivation seen in Fig. 1c was studied via post-catalytic characterization. Both the XRD and TEM (Fig. S32 and Fig. S33, respectively) show similar particle size and crystallinity to their fresh catalyst counterparts, so this is not the reason for deactivation. The EDX images seen in Fig. S34 show a homogenous concentration of nickel throughout the catalyst so particle agglomeration does not occur for the 33.1% Ni TiO_x catalyst, implying this may not be the reason for the deactivation. However, for the 6.9%, 14.1%, and 24.6% Ni TiO_x catalysts, deactivation might be occurring due to particle agglomeration. These agglomerations occurring are possibly due to the nickel loading versus surface area. From the BET surface area (Table 4) there is an increase in surface area by ~ 30 m^2/g when increasing the nickel content from 6.9% to 14.1%, this increase in surface area possibly allows for a more dispersed nickel as the nickel has more space to occupy, leading to a less sintered catalyst. This can also explain why the Ni particles in 6.9% and 24.6% Ni TiO_x agglomerate as their surface area is nearly identical to the lower loaded Ni catalysts (1.5% and 14.1% respectively). This lack of change in surface area means the increased nickel content is confined in a similar surface area, allowing for more nickel to interact and thus agglomerate during the reaction. The reason why 33.1% Ni TiO_x shows no particle agglomeration is due to its enhanced surface area, as the nickel content increases, the surface area triples, possibly allowing for more dispersed nickel. The H_2 TPD seen in Figs. S47–S49, shows that 33.1% Ni TiO_x has the highest chemisorbed H_2 peak, with 14.1% and 24.6% having similar H_2 peaks to each other. When these H_2 amounts are normalized to amount of nickel in the catalyst, the highest chemisorbed H_2 is 33.1% Ni TiO_x and the lowest chemisorbed H_2 is 24.6% Ni TiO_x. Using H_2 chemisorption is useful as generally the higher the metal dispersion, the higher the chemisorbed H_2 [48]. From these data, the sintering from 24.6% Ni TiO_x arises from the lack of metal dispersion, while the enhanced stability of 33.1% Ni TiO_x is due to having the highest metal dispersion.

Furthermore the sintering in 24.6 Ni TiO_x can be observed in the elemental map (Fig. S50) where there is a homogenous amount of oxygen on the surface of the catalyst, reinforcing that the nickel agglomeration seen is possibly Ni^0. Oxidation states can further be determined via XPS, where when comparing the fresh and used XPS spectra, only one obvious change is observed in the Ni 2p region. This occurs in 24.6% Ni TiO_x (Fig. 6 , Fig. 9), where during the process of the reaction, nickel oxide gets reduced to Ni^0. This is seen by an additional peak appearing at around 852 eV. This indicates that the nickel clusters seen in the EDX of 24.6% Ni TiO_x (Fig. S34) were Ni^0 and not agglomerations of nickel oxide. This means that 24.6% Ni TiO_x is probably the least stable of all the catalysts due to Ni^0 formation during the reaction. While there is an agglomeration of nickel in 6.9% and 14.1% Ni TiO_x, these agglomerations are not highly concentrated enough to see a nickel peak in the XPS 2p region implying greater stability than 24.6% Ni TiO_x. There is no Ni^0 peak seen in the XPS spectra of 33.1% Ni TiO_x meaning that the catalyst is more stable than 24.6% Ni TiO_x. This additional stability likely comes from the $NiTiO_3$ phase that is seen in Raman (Fig. 5) for 33.1% $NiTiO_3$.

The Raman spectra in Fig. 5 and Fig. 8a show changes from the pre-reaction and post-reaction catalysts. Some nodes disappear after the reaction for the Ni TiO_x catalyst, and all the other catalysts gain two peaks at 1350 and 1600 cm^{-1} which correlate with carbonaceous species. These carbonaceous species are not seen in TEM, however. It was observed that the catalysts that had higher conversions also had higher carbonaceous species deposition. However, this does not mean that the carbonaceous species catalytically aid in the reaction, as the 24.6% and 33.1% Ni TiO_x catalysts have similar carbon deposition amounts, but have drastically different conversions.

TPD (Figs. S39–S43) studies on the post- reaction catalysts agree with the Raman data, in which all the catalysts show an excess of CO and CO_2 that come off around 400–450 °C, which is not in the pre-reaction catalyst TPD. This excess of CO and CO_2 is likely from the carbonaceous species deposited on the catalyst during the reaction. The only catalyst that shows a significant amount of isobutylene coming off during the TPD is 33.1% Ni TiO_x where at 200 °C isobutylene, H_2O, CO, and O_2 come off the catalyst. This may imply that the excess CO removal is from the carbonaceous species on the catalyst. Using CO_2 TGA the CO_2 formed during the reaction would not be poisonous to the catalyst, as seen in Fig. S44 where weight loss from CO_2 was regained during the reaction. Additionally, from TPD (Figs. S37–43), H_2O on the catalyst is formed during the reaction. Water is known to deactivate nickel based catalysts through the transformation of Ni to NiOH [49,50]. In other cases water has been observed to cause sintering, which can further cause coking [51]. From the post-reaction Raman (Fig. 8), the formed $NiTiO_3$ phases get removed during the reaction, and this phase loss could possibly weaken the interactions between Ni and TiO_x. This loss of phase may be an additional reason for catalytic deactivation. However, from the above studies, deactivation is occurring due to formation of carbonaceous species and water during the reaction, as well as the loss of the $NiTiO_3$ phase.

4.4. Catalytic regeneration

From the TPD (Figs. S39–43), H_2O is lost at ~ 200 °C and ~ 400 °C. Due to this, 33.1% Ni TiO_x was calcined at 450 °C overnight in order to get rid of the excess H_2O to observe if the catalyst can be regenerated. Table S2 shows that after re-calcination, the catalyst can be regenerated and reused with similar activity as its fresh counterpart. These regenerated catalysts were regenerated two more times showing that the catalyst can be reused multiple times. It is possible that from the re-calcinations, the $NiTiO_3$ phase and oxygen vacancies regenerate

enabling similar conversions.

5. Conclusions

In this study, various nickel doped titanium oxides were able to facilitate the partial oxidation of isobutylene. The 14.1% and 33.1% Ni TiO_x catalysts were shown to catalyze this reaction with high selectivity towards two valuable liquid products. The 14.1% Ni TiO_x catalysts produces isoprene, and the 33.1% Ni TiO_x catalyst generates p-xylene. Isoprene is of particular interest which can produced in this reaction without the need of formaldehyde as a co-reactant. Catalytic deactivation was seen to be a problem; however, this catalyst can be regenerated with near identical conversion, showing this catalyst can be useful in the partial oxidation of isobutylene.

CRediT author contribution statement

SM, PN, and SLS in experimental design, SM synthesized/characterized materials, and conducted experiments. LP performed XRF and BET on catalysts. IP aided in TPD, XPS, and NMR analysis. TK preformed NMR and aided in initial GC analysis. PK helped in the analysis of XPS on the catalysts. Paper was written with the aid of SM, PN, and SLS, with P. N and S.L.S being project leads. All authors have read and approved the final paper.

Declaration of Competing Interest

The authors declare that they have no known competing financial interests or personal relationships that could have appeared to influence the work reported in this paper.

Acknowledgment

We acknowledge the support of this work from ExxonMobil Research and Engineering Company. TEM was done using the UConn/Thermo Fisher Scientific Center for Advanced Microscopy and Materials Analysis (CAMMA). We acknowledge the US Department of Energy, Office of Basic Energy Sciences, Division of Chemical, Biological and Geological Sciences under grant DE- FG02-86ER13622. A000 for partial support of this research. We also thank Peter Kerns for aid in XPS analysis.

Appendix A. Supporting information

Supplementary data associated with this article can be found in the online version at doi:10.1016/j.apcatb.2021.120711.

References

[1] R.K. Grasselli, Advances and future trends in selective oxidation and ammoxidation catalysis, Catal. Today 49 (1–3) (1999) 141–153, https://doi.org/10.1016/S0920-5861(98)00418-0.
[2] S. Sengodan, R. Lan, J. Humphreys, D. Du, W. Xu, H. Wang, S. Tao, Advances in reforming and partial oxidation of hydrocarbons for hydrogen production and fuel cell applications, Renew. Sustain. Energy Rev. (2018) 761–780, https://doi.org/10.1016/j.rser.2017.09.071.
[3] E. Sahle-Demessie, M. Gonzalez, Z.-M. Wang, P. Biswas, Synthesizing alcohols and ketones by photoinduced catalytic partial oxidation of hydrocarbons in TiO2 film reactors prepared by three different, Methods (1999), https://doi.org/10.1021/ie990054l.
[4] V.C. Corberán, A. Corma, G. Kremenić, Kinetics of the partial oxidation of isobutene over silica-supported molybdenum-uranium oxide catalyst, Ind. Eng. Chem. Prod. Res. Dev. 24 (1) (1985) 62–68, https://doi.org/10.1021/i300017a012.
[5] N. Song, C. Rhodes, J.K. Bartley, S.H. Taylor, D. Chadwick, G.J. Hutchings, Oxidation of isobutene to methacrolein using bismuth molybdate catalysts: comparison of operation in periodic and continuous feed mode, J. Catal. 236 (2) (2005) 282–291, https://doi.org/10.1016/j.jcat.2005.10.008.
[6] M.D. Robbins, M.A. Henderson, The partial oxidation of isobutene and propene on TiO2(110), J. Catal. 238 (1) (2006) 111–121, https://doi.org/10.1016/j.jcat.2005.11.041.
[7] M.W. Peters, J.D. Taylor, M. Jenni, L.E. Manzer, D.E. Henton, Integrated ProcessTo Selectively Convert Renewable Isobutanol To P-Xylene, 2009, 1(19). ⟨https://doi.org/WO2011044243A1⟩.
[8] M. Cheng, H. Zhao, J. Yang, J. Zhao, L. Yan, H. Song, L. Chou, The catalytic dehydrogenation of isobutane and the stability enhancement over Fe incorporated SBA-15, Microporous Mesoporous Mater. 266 (2018) 117–125, https://doi.org/10.1016/j.micromeso.2018.02.046.
[9] S. Breiter, H.G. Lintz, Partial oxidation of isobutene to methacrolein on BiW/FeCoMoK mixed oxide catalysts, Chem. Eng. Sci. 50 (5) (1995) 785–791, https://doi.org/10.1016/0009-2509(94)00458-4.
[10] J. Gao, G. Fan, L. Yang, X. Cao, P. Zhang, F. Li, Oxidative esterification of methacrolein to methyl methacrylate over gold nanoparticles on hydroxyapatite, ChemCatChem 9 (7) (2017) 1230–1241, https://doi.org/10.1002/cctc.201601560.
[11] H. Zhang, R. Yan, L. Yang, Y. Diao, L. Wang, S. Zhang, Investigation of Cu-and Fe-Doped CsH3PMo11VO40 heteropoly compounds for the selective oxidation of methacrolein to methacrylic acid, Ind. Eng. Chem. Res. 52 (12) (2013) 4484–4490, https://doi.org/10.1021/ie3032718.
[12] J. Guan, K. Song, H. Xu, Z. Wang, Y. Ma, F. Shang, Q. Kan, Oxidation of isobutane and isobutene to methacrolein over hydrothermally synthesized Mo-V-Te-O mixed oxide catalysts, Catal. Commun. 10 (5) (2009) 528–532, https://doi.org/10.1016/j.catcom.2008.10.025.
[13] C.L. Williams, C.-C. Chang, P. Do, N. Nikbin, S. Caratzoulas, D.G. Vlachos, R. F. Lobo, W. Fan, P.J. Dauenhauer, Analysis of the immune response to Neisseria meningitidis using a proteomics approach, Methods Mol. Biol. 799 (2012) 343–360, https://doi.org/10.1021/cs300011a.
[14] P. Raghavendrachar, S. Ramachandran, Liquid-Phase Catalytic Oxidation of p-Xylene*, 1992, Vol. 31.
[15] P.P. Van Uytvanck, G. Haire, P.J. Marshall, J.S. Dennis, Impact on the polyester value chain of using P-xylene derived from biomass, ACS Sustain. Chem. Eng. 5 (5) (2017) 4119–4126, https://doi.org/10.1021/acssuschemeng.7b00105.
[16] S. Garrat, A.G. Carr, G. Langstein, M. Bochmann, Isobutene polymerization and isobutene-isoprene copolymerization catalyzed by cationic zirconocene hydride complexes, Macromolecules 36 (12) (2003) 4276–4287, https://doi.org/10.1021/ma034320p.
[17] Y. Qi, L. Cui, Q. Dai, Y. Li, C. Bai, Assembly line synthesis of isoprene from formaldehyde and isobutene over SiO2-supported MoP catalysts with active deposited carbon, RSC Adv. 7 (59) (2017) 37392–37401, https://doi.org/10.1039/c7ra05078j.
[18] R. Del Rosso, C. Mazzocchia, P. Centola, Oxidation of isobutene over cuprous oxide between 400 and 550 °C, React. Kinet. Catal. Lett. 9 (1) (1978) 23–27, https://doi.org/10.1007/BF02070363.
[19] V.L. Sushkevich, V.V. Ordomsky, I.I. Ivanova, Synthesis of isoprene from formaldehyde and isobutene over phosphate catalysts, Appl. Catal. A Gen. 441–442 (2012) 21–29, https://doi.org/10.1016/j.apcata.2012.06.034.
[20] H. Zhu, R. Zhang, Q. Wang, S. Xu, Insighting into the effect of acid sites on the catalytic performance of HZSM-5 during the one-step preparation of isoprene by formaldehyde and isobutene, Catal. Lett. 151 (2) (2021) 435–444, https://doi.org/10.1007/s10562-020-03306-9.
[21] O.A. Ponomareva, D.L. Chistov, P.A. Kots, V.R. Drozhzhin, L.I. Rodionova, I. I. Ivanova, Isoprene synthesis from formaldehyde and isobutylene in the presence of aluminum- and niobium-containing BEA catalysts, Pet. Chem. 60 (8) (2020) 942–949, https://doi.org/10.1134/S0965544120080125.
[22] Q. Wang, X. Luo, L. Liu, S. Tao, S. Xu, Study on heteropolyacid-based catalysts with high activity and reusability for isoprene synthesis from formaldehyde and isobutene, New J. Chem. 45 (12) (2021) 5371–5381, https://doi.org/10.1039/d0nj05305h.
[23] D. Weber, P. Weidler, B. Kraushaar-Czarnetzki, Partial oxidation of isobutane and isobutene to methacrolein over a novel Mo–V–Nb(–Te) mixed oxide catalyst, Top. Catal. 60 (17–18) (2017) 1401–1407, https://doi.org/10.1007/s11244-017-0830-0.
[24] J. Liu, G. Wang, X. Zhu, C. Li, H. Shan, Temperature-programmed studies of isobutene oxidation over α-Bi2Mo3O12: active oxygen species and reaction mechanism, Appl. Surf. Sci. 470 (2019) 846–853, https://doi.org/10.1016/j.apsusc.2018.11.187.
[25] E.M. Gaigneaux, M.J. Genet, P. Ruiz, B. Delmon, Catalytic behavior of molybdenum suboxides in the selective oxidation of isobutene to methacrolein, J. Phys. Chem. B 104 (24) (2000) 5724–5737, https://doi.org/10.1021/jp9913416.
[26] L. Moens, P. Ruiz, B. Delmon, M. Devillers, Cooperation effects towards partial oxidation of isobutene in multiphasic catalysts based on bismuth pyrostannate, Appl. Catal. A Gen. 171 (1) (1998) 131–143, https://doi.org/10.1016/S0926-860X(98)00075-1.
[27] M. Volanti, D. Cespi, F. Passarini, E. Neri, F. Cavani, P. Mizsey, D. Fozer, Terephthalic acid from renewable sources: early-stage sustainability analysis of a Bio-PET precursor, Green Chem. 21 (4) (2019) 885–896, https://doi.org/10.1039/C8GC03666G.
[28] A.F. Lee, P. Sears, S.D. Pollington, J. Matthey, T. Overton, P.J. Sears, T.L. Overton, P.B. Wells, D.F. Lee, Synergic interactions in a urania-titania catalyst for isobutene partial oxidation heterogeneous catalysis for biofuels production view project batch to continuous view project synergic interactions in a urania-titania catalyst for isobutene partial oxidation, Catal. Lett. 70 (2000) 183–186, https://doi.org/10.1023/A:1018801804706.
[29] D.A. Kriz, Q.A. Nizami, J. He, T. Jafari, Y. Dang, P. Kerns, A.G. Meguerdichian, S. L. Suib, P. Nandi, Partial oxidation of methane to synthesis gas using supported ga-

containing bimetallic catalysts and a Ti-promoter, ChemCatChem 10 (19) (2018) 4300–4308, https://doi.org/10.1002/cctc.201801030.
[30] V.M. Shinde, G. Madras, Catalytic performance of highly dispersed Ni/TiO_2 for dry and steam reforming of methane, RSC Adv. 4 (10) (2014) 4817–4826, https://doi.org/10.1039/c3ra45961f.
[31] Y. Shen, A.C. Lua, Sol-gel synthesis of titanium oxide supported nickel catalysts for hydrogen and carbon production by methane decomposition, J. Power Sources 280 (2015) 467–475, https://doi.org/10.1016/j.jpowsour.2015.01.057.
[32] D. Hu, C. Liu, L. Li, K. Lv, Le, Y.H. Zhang, J.L. Li, Carbon dioxide reforming of methane over nickel catalysts supported on TiO2(001) nanosheets, Int. J. Hydrogen Energy 43 (46) (2018) 21345–21354, https://doi.org/10.1016/j.ijhydene.2018.09.188.
[33] M. Pudukudy, Z. Yaakob, A. Kadier, M.S. Takriff, N.S.M. Hassan, One-pot sol–gel synthesis of Ni/TiO2 catalysts for methane decomposition into COx free hydrogen and multiwalled carbon nanotubes, Int. J. Hydrogen Energy 42 (26) (2017) 16495–16513, https://doi.org/10.1016/j.ijhydene.2017.04.223.
[34] E.T. Kho, J. Scott, R. Amal, Ni/TiO2 for low temperature steam reforming of methane, Chem. Eng. Sci. 140 (2016) 161–170, https://doi.org/10.1016/j.ces.2015.10.021.
[35] A.E. Awadallah, M.S. Mostafa, A.A. Aboul-Enein, S.A. Hanafi, Hydrogen production via methane decomposition over Al2O3-TiO2 binary oxides supported Ni catalysts: effect of Ti content on the catalytic efficiency, Fuel 129 (2014) 68–77, https://doi.org/10.1016/j.fuel.2014.03.047.
[36] H. Olivier-Bourbigou, P.A.R. Breuil, L. Magna, T. Michel, M.F.E. Pastor, D. Delcroix, Nickel catalyzed olefin oligomerization and dimerization, Chem. Rev. 120 (15) (2020) 7919–7983, https://doi.org/10.1021/ACS.CHEMREV.0C00076.
[37] B. Dutta, R. Clarke, S. Raman, T.D. Shaffer, L. Achola, P. Nandi, S.L. Suib, Lithium promoted mesoporous manganese oxide catalyzed oxidation of allyl ethers, Nat. Commun. 10 (1) (2019) 1–6, https://doi.org/10.1038/s41467-019-08619-x.
[38] B. Dutta, S. Biswas, V. Sharma, N.O. Savage, S.P. Alpay, S.L. Suib, Mesoporous manganese oxide catalyzed aerobic oxidative coupling of anilines to aromatic azo compounds, Angew. Chem. - Int. Ed. 55 (6) (2016) 2171–2175, https://doi.org/10.1002/anie.201508223.
[39] B. Dutta, S. March, L. Achola, S. Sahoo, J. He, A. Shirazi Amin, Y. Wu, S. Poges, S. Pamir Alpay, S.L. Suib, Mesoporous cobalt/manganese oxide: a highly selective bifunctional catalyst for amine-imine transformations, Green Chem. 20 (14) (2018) 3180–3185, https://doi.org/10.1039/c8gc00862k.
[40] S. Biswas, H.S. Khanna, Q.A. Nizami, D.R. Caldwell, K.T. Cavanaugh, A.R. Howell, S. Raman, S.L. Suib, P. Nandi, Heterogeneous catalytic oxidation of amides to imides by manganese oxides, Sci. Rep. 8 (1) (2018) 1–8, https://doi.org/10.1038/s41598-018-31729-3.
[41] C. Weerakkody, S. Biswas, W. Song, J. He, N. Wasalathanthri, S. Dissanayake, D. A. Kriz, B. Dutta, S.L. Suib, Controllable synthesis of mesoporous cobalt oxide for peroxide free catalytic epoxidation of alkenes under aerobic conditions, Appl. Catal. B Environ. 221 (2018) 681–690, https://doi.org/10.1016/j.apcatb.2017.09.053.
[42] Alexander V. Naumkin, Anna Kraut-Vass, Stephen W. Gaarenstroom, C.J.P. NIST X-Ray, Photoelectron spectroscopy database, Meas. Serv. Div. Natl. Inst. Stand. Technol. 20899 (20) (2012) 20899, https://doi.org/10.18434/T4T88K.
[43] A.P. Grosvenor, M.C. Biesinger, R.S.C. Smart, N.S. McIntyre, New interpretations of XPS spectra of nickel metal and oxides, Surf. Sci. 600 (9) (2006) 1771–1779, https://doi.org/10.1016/j.susc.2006.01.041.
[44] J. Zheng, J. Ye, M.A. Ortuño, J.L. Fulton, O.Y. Gutiérrez, D.M. Camaioni, R. K. Motkuri, Z. Li, T.E. Webber, B.L. Mehdi, N.D. Browning, R.L. Penn, O.K. Farha, J.T. Hupp, D.G. Truhlar, C.J. Cramer, J.A. Lercher, Selective methane oxidation to methanol on Cu-Oxo dimers stabilized by zirconia nodes of an NU-1000 metal-organic framework, J. Am. Chem. Soc. 141 (23) (2019) 9292–9304, https://doi.org/10.1021/jacs.9b02902.
[45] S.A. Bilmes, P. Mandelbaum, F. Alvarez, N.M. Victoria, Surface and Electronic Structure of Titanium Dioxide Photocatalysts, 2000. ⟨https://doi.org/10.1021/jp0010132⟩.
[46] S.V. Gnedenkov, S.L. Sinebryukhov, V.V. Zheleznov, D.P. Opra, E.I. Voit, E. B. Modin, A.A. Sokolov, Yu, A. Ustinov, V.I. Sergienko, Effect of Hf-doping on electrochemical performance of anatase TiO_2 as an anode material for lithium storage, R. Soc. Open Sci. 5 (6) (2018), 171811, https://doi.org/10.1098/rsos.171811.
[47] S. Li, C. Zhu, S. Guo, L. Guo, A dispersed rutile-TiO2-supported Ni nanoparticle for enhanced gas production from catalytic hydrothermal gasification of glucose, RSC Adv. 5 (100) (2015) 81905–81914, https://doi.org/10.1039/C5RA12025J.
[48] F. Drault, C. Comminges, F. Can, L. Pirault-Roy, F. Epron, A. Valant, Palladium, iridium, and rhodium supported catalysts: predictive H_2 chemisorption by statistical cuboctahedron clusters model, Materials 11 (5) (2018), https://doi.org/10.3390/MA11050819.
[49] W. Lin, H. Cheng, J. Ming, Y. Yu, F. Zhao, Deactivation of Ni/TiO_2 catalyst in the hydrogenation of nitrobenzene in water and improvement in its stability by coating a layer of hydrophobic carbon, J. Catal. 291 (2012) 149–154, https://doi.org/10.1016/J.JCAT.2012.04.020.
[50] Y.C. Chiou, U. Kumar, J.C.S. Wu, Photocatalytic splitting of water on NiO/$InTaO_4$ catalysts prepared by an innovative sol–gel method, Appl. Catal. A Gen. 357 (1) (2009) 73–78, https://doi.org/10.1016/J.APCATA.2009.01.016.
[51] G.L. Bezemer, T.J. Remans, A.P. Bavel, A.I. van; Dugulan, Direct evidence of water-assisted sintering of cobalt on carbon nanofiber catalysts during simulated Fischer–Tropsch conditions revealed with in situ Mössbauer spectroscopy, J. Am. Chem. Soc. 132 (25) (2010) 8540–8541, https://doi.org/10.1021/JA103002K.
[52] Anton A. Gabrienko, Zoya N. Lashchinskaya, Sergei S. Arzumanov, Alexander V. Toktarev, Dieter Freude, Jürgen Haase, Alexander G. Stepanov, Alexander G. Stepanov, Isobutene Transformation to Aromatics on Zn-Modified Zeolite: Particular Effects of Zn^{2+} and ZnO Species on the Reaction Occurrence Revealed with Solid-State NMR and FTIR Spectroscopy, The Journal of Physical Chemistry 125 (28) (2021) 15343–15353, https://doi.org/10.1021/acs.jpcc.1c04249. In press.